Article

Integration of Multi-Source Datasets for Assessing Ground Swelling/Shrinking Risk in Cyprus: The Case Studies of Pyrgos–Parekklisia and Moni

Athanasios V. Argyriou [1,2], Maria Prodromou [1,3], Christos Theocharidis [1,3], Kyriaki Fotiou [1,3], Stavroula Alatza [4], Constantinos Loupasakis [5], Zampela Pittaki-Chrysodonta [1], Charalampos Kontoes [4], Diofantos G. Hadjimitsis [1,3] and Marios Tzouvaras [1,3,*]

[1] ERATOSTHENES Centre of Excellence, Limassol 3012, Cyprus; nasos@ims.forth.gr (A.V.A.); maria.prodromou@eratosthenes.org.cy (M.P.); christos.theocharidis@eratosthenes.org.cy (C.T.); kyriaki.fotiou@eratosthenes.org.cy (K.F.); zampela.pittaki@eratosthenes.org.cy (Z.P.-C.); d.hadjimitsis@cut.ac.cy (D.G.H.)

[2] Laboratory of Geophysical-Satellite Remote Sensing & Archaeoenvironment (GeoSat ReSeArch Lab), Institute for Mediterranean Studies, Foundation for Research and Technology Hellas (FORTH), 74100 Rethymno, Greece

[3] Department of Civil Engineering and Geomatics, Cyprus University of Technology, Limassol 3036, Cyprus

[4] National Observatory of Athens, Operational Unit BEYOND Centre for Earth Observation Research and Satellite Remote Sensing IAASARS/NOA, 15236 Athens, Greece; alatza@noa.gr (S.A.); kontoes@noa.gr (C.K.)

[5] Laboratory of Engineering Geology and Hydrogeology, School of Mining and Metallurgical Engineering, National Technical University of Athens, 15780 Athens, Greece; cloupasakis@metal.ntua.gr

* Correspondence: marios.tzouvaras@eratosthenes.org.cy; Tel.: +357-25002006

Citation: Argyriou, A.V.; Prodromou, M.; Theocharidis, C.; Fotiou, K.; Alatza, S.; Loupasakis, C.; Pittaki-Chrysodonta, Z.; Kontoes, C.; Hadjimitsis, D.G.; Tzouvaras, M. Integration of Multi-Source Datasets for Assessing Ground Swelling/ Shrinking Risk in Cyprus: The Case Studies of Pyrgos–Parekklisia and Moni.

Academic Editors: Bahareh Kalantar, Alfian Abdul Halin and Husam A. H. Al-Najjar

Received: 18 July 2024
Revised: 18 August 2024
Accepted: 21 August 2024
Published: 28 August 2024

Abstract: The determination of swelling/shrinking phenomena, from natural and anthropogenic activity, is examined in this study through the synergy of various remote sensing methodologies. For the period of 2016–2022, a time-series InSAR analysis of Sentinel-1 satellite images, with a Coherent Change Detection procedure, was conducted to calculate the Normalized Coherence Difference. These were combined with Sentinel-2 multispectral data by exploiting the Normalized Difference Vegetation Index to create multi-temporal image composites. In addition, ALOS-Palsar DEM derivatives highlighted the geomorphological characteristics, which, in conjunction with the satellite imagery outcomes and other auxiliary spatial datasets, were embedded within a MultiCriteria Decision Analysis (MCDA) model. The synergy of the remote sensing and GIS techniques' applicability within the MCDA model highlighted the zones undergoing seasonal swelling/shrinking processes in Pyrgos–Parekklisia and Moni regions in Cyprus. The accuracy assessment of the produced final MCDA outcome provided an overall accuracy of 72.4%, with the Kappa statistic being 0.66, indicating substantial agreement of the MCDA outcome with the results from a Persistent Scatterer Interferometry analysis and ground-truth observations. Thus, this study offers decisionmakers a powerful procedure to monitor longer- and shorter-term swelling/shrinking phenomena.

Keywords: data fusion; optical; SAR; geohazards observatory; multi-criteria decision analysis

the correlation between infrastructure damage and the moisture content beneath various geological formations, particularly expansive clays [1–4]. Remote sensing stands as a pivotal approach, providing extensive coverage and indispensable insights for assessing slope failure, stability, and the consequent occurrence of landslides and subsidence [5–7]. However, there remains a scarcity of studies employing interdisciplinary Earth Observation (EO) technologies to evaluate swelling and shrinkage effects in conjunction with ground movements [8,9].

1. Introduction

Surface deformation represents a significant geohazard with far-reaching implications worldwide. The deformation of the Earth's surface can cause a multitude of short- and long-term effects on ecosystems, infrastructure, and human populations. It often arises from natural phenomena like earthquakes or human-induced activities such as mining and groundwater extraction. Despite this, there are many cases where the causal factor of surface deformation, such as subsidence and sinking of the ground, is soil saturation by water, which leads to the loss of structural integrity and slope failure. There are numerous studies worldwide—both numerical and experimental—endeavoring to discern

Consequently, there exists an opportunity for a comprehensive evaluation of available EO technologies and their amalgamation to enable decision-makers to advance and devise a robust methodological framework for elucidating the intricate interplay between ground moisture and seasonal swelling and shrinking effects. InSAR radar satellite datasets have emerged as a prevalent tool for evaluating ground movements in relation to urbanization, land-use patterns, and geotechnical considerations [10–12]. The Coherent Change Detection (CCD) technique is widely used for the identification and analysis of fast-moving land displacement events through radar satellite images, since the information related to the changes in topography between two or more images over time is considered crucial. The coherence variable describes and measures the quality of each produced interferogram in the InSAR methodology [13].

A range of applications have proven the potential of the CCD methodology to verify the detection of rapid displacement phenomena due to natural hazards [14], such as earthquakes [15,16] and landslides [17]. Also, SAR interferometry is widely used in a variety of natural [18–29] and human-induced [30–35] surface displacement detection and monitoring applications. Slow-moving deformation phenomena can be detected by InSAR time-series, which aim to detect coherent stable scatterers over time through diverse techniques, such as Persistent Scatterer Interferometry (PSI) [36] and Small Baseline Subset (SBAS) [37]. Based on these techniques, various studies have identified and determined diverse types of ground deformation, including landslides, ground water extraction, and volcanic and tectonic activity [38–40].

Furthermore, complementary to EO technologies, geoinformatics methodologies are used extensively to analyze diverse factors directly or indirectly associated with swelling and shrinking phenomena by assessing various geomorphometric characteristics [41–43]. These characteristics serve to elucidate the interconnectedness of geological formations, soil properties, and hydrological processes, thereby offering valuable insights into their relationship with ground movements, soil moisture, and swelling/shrinking effects. Moreover, geoinformatics enables the examination of diverse spatial decision problems through Multi-Criteria Decision Analysis (MCDA) [44,45]. By integrating geographical datasets, these approaches facilitate informed judgments to attain a comprehensive assessment of decision criteria [46]. Consequently, decision-makers can leverage MCDA to devise geospatial solutions for issues contingent upon multiple criteria [47,48].

Understanding the causes, impacts, and risks associated with surface deformation is crucial for effective hazard mitigation, land-use planning, and disaster resilience efforts globally and in regions like Cyprus, where geohazards pose significant challenges and risks. Cyprus is located in a seismically active region experiencing surface deformation from natural processes but also by subsidence phenomena, especially in coastal areas, related to groundwater extraction for agriculture and urban development, leading to land subsidence, saltwater intrusion, and coastal erosion. The Coherent Change Detection (CCD) technique has been applied successfully in multiple case studies in Cyprus [49–51].

The present study aims to highlight the efficiency of integrating the aforementioned diverse methods within a multidisciplinary approach, by combining EO and geoinformatics to be applied throughout the Area of Interest (AoI) of Pyrgos–Parekklisia and to identify specific problematic areas related to swelling/shrinking phenomena [52] (Figure 1) and investigate the capability of an efficient risk management system in Cyprus.

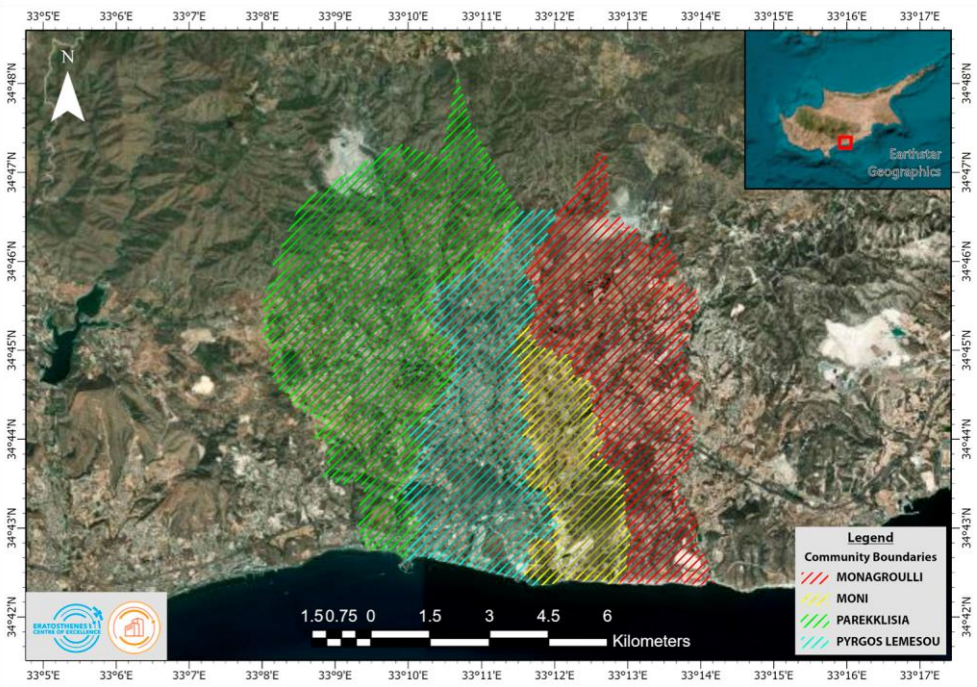

Figure 1. The Pyrgos–Parekklisia, Moni, and Monagroulli deforming sites in Limassol, Cyprus.

The villages of Pyrgos and Parekklisia are located in Limassol District, in the south of the Republic of Cyprus, and more specifically on the eastern outskirts of Limassol city. They are situated, respectively, at an altitude of 75 m and 120 m above mean sea level, on weathered upper and lower pillow lavas alternating to the zeolitic phase (bentonitic clays with silt and radiolarite intercalations) [53,54]. These are the bentonitic clays from the Kathikas, Moni, Kannaviou, and Pera Pedi geological formations (Figure 2). These soils, especially from Kannaviou and Moni formations, are characterized by high plasticity, and thus, high potential for swelling/shrinking occurrence that can affect all of the above structures [55].

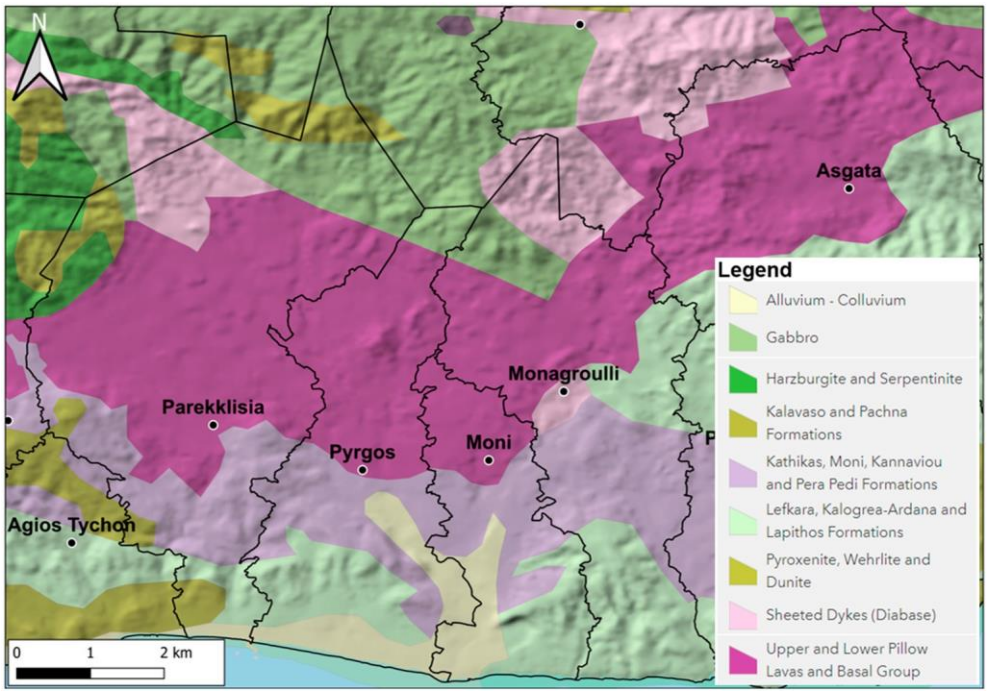

Figure 2. The Pyrgos Lemesou–Parekklisia and Moni–Monagroulli geology.

2. Materials and Methods

This study utilized both radar and optical satellite imagery to analyze surface deformation phenomena, using free, open-source software, such as SNAP 9.0, QGIS 3.34.4, and Google Earth Engine (GEE). In addition to these primary datasets, various auxiliary datasets were incorporated

to provide comprehensive insights into the factors influencing surface deformation. These auxiliary datasets encompassed a range of geospatial information, including geomorphological features, morphotectonic characteristics, soil properties, and hydro-lithological attributes. By integrating these diverse datasets, this study aimed to capture the complex interplay between geological, hydrological, and environmental factors contributing to surface deformation processes, especially due to the swelling and shrinking effect. All the datasets were considered as factors which are related indirectly or directly to the deformation and motion of the ground. Thus, examining their interrelationships within a GIS environment can highlight aspects of hazardous landscape deformation zones.

2.1. Coherent Change Detection

A Sentinel-1 Single-Look Complex (SLC) dataset was used for the Coherent Change Detection (CCD) analysis, comprising 136 ascending and 136 descending satellite images obtained during the period 2016–2022 (Figure 3).

Figure 3. Sentinel-1 satellite passes in ascending and descending tracks and satellite image details.

The CCD processing was carried out using the Sentinel Application Platform (SNAP) software (Version 8.0). As presented in Figure 4, the processing methodology was divided into two different sections. The first section concerned the pre-processing of the used dataset. Initially, the selection of the master and the slave images was carried out, as well as the splitting of both images in the respective Area of Interest (AoI). This step was followed by the application of their orbital information. Following the preprocessing section, the second section included several steps for the estimation of the coherence variable. It is noted that the SRTM-1Sec DEM was used for the steps of Back-Geocoding and Terrain Correction [56]. Finally, every result of the processed pairs of images, including the coherence variable, was exported as a GeoTiff file for further analysis. It is also noted that the CCD workflow methodology was used for both ascending and descending datasets.

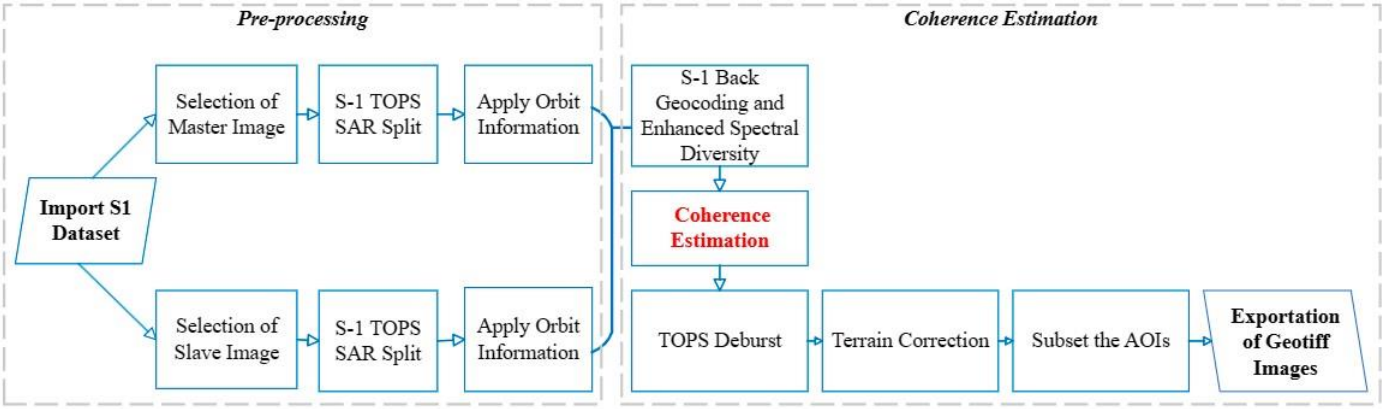

Figure 4. The Coherent Change Detection workflow methodology. The step that provides the coherence values is marked in red.

The creation of the coherence images was followed by a post-processing procedure that was implemented in R software (version 4.3.0) to generate the Coherence Difference and the Normalized Coherence difference. This process utilizes the "rgdal" package and other packages such as "terra", "sp", "dplyr", and "matrixstats". Firstly, the shapefiles of the AoIs were defined in the same coordinate system as the raster files (coherence images), ensuring spatial alignment between the shapefiles and the images. Next, each coherence image was resampled using the nearest neighbour method to match the extent and resolution of the other images. This procedure ensured consistency in the images' spatial properties. Subsequently, a mask was created to crop all the images based on the boundaries of the
AoIs for both satellite passes (ascending and descending). Then, the coherence difference and the normalized coherence difference were calculated from Equations (1) and (2), where X_1 and X_2 are the coherence values of the first and second image pairs, respectively.

$$\Delta X = X_2 - X_1 \quad (1)$$

$$\text{Normalized } \Delta X = \frac{X^2 - X_1}{X_2 + X_1} \quad (2)$$

Furthermore, a classification scheme to categorize areas/pixels based on their coherence values and confidence levels was applied. The classification was performed utilizing deviations from the mean values of the coherence data. First, areas/pixels with coherence values below the lower confidence limit (i.e., three standard deviations from the mean) were identified as areas with a very high probability of changes occurring. Next, the normalized coherence difference values within the range of two to three standard deviations from the mean were classified as "High"-probability areas, indicating a high likelihood of land change occurrence. The "Medium–Low" class included values falling between one and two standard deviations from the mean. Values within one standard deviation, both positive and negative, from the mean value were classified as "Very Low–None". This class contained areas with no possibility of land change or any other natural change, as well as positive values indicating a coherence increase. The conditions utilized to classify all values are presented in Equation (3) below, where μ is the mean value and σ is the standard deviation of each dataset.

$$\text{"Very High"} \leq \mu - 3\sigma \leq \text{"High"} \leq \mu - 2\sigma \leq \text{"Medium–Low"} \leq \mu - 1\sigma \leq \text{"Very Low–None"} \quad (3)$$

An aspect map was generated from the ALOSPalsar Digital Elevation Models (DEMs) (12.5 m spatial resolution) that focuses solely on the aspect directions SE, E, and NE (22.5–157.5 degrees) and SW, W, and NW (202.5–337.5 degrees) within the study area. These specific aspect directions align with SAR images acquired from descending and ascending orbits, respectively, resulting in the retention of only the non-shaded areas, which correspond to the selected aspects for the analysis, while all other aspects were masked out.

2.2. Optical Data

This section aims to utilize multispectral Sentinel-2 imagery with a spatial resolution of 10 m, and the computational power of the GEE platform. Specifically, Sentinel-2 level-2A cloud-free satellite data were utilized, covering the period 2017–2022, to create seasonal image composites per year. Furthermore, for all image composites, the Normalized Difference Vegetation Index (NDVI) was calculated and added as a new band to the image composites. The NDVI was calculated, as it is one of the most common vegetation indices that have been used in the wider literature and identifies vegetation changes [57,58]. The values range from −1 to +1, where higher values indicate healthier vegetation and lower values indicate no vegetated features, such as barren surfaces (rock and soil), water, snow, ice, and clouds. The NDVI was proposed by Tucker [59] and is calculated based on Equation (4) below.

$$NDVI = \frac{NIR - RED}{NIR + RED} \quad (4)$$

NIR refers to the near-infrared band, whereas RED refers to the red band (central wavelength for Sentinel-2: 0.842 µm). Regarding swelling phenomena, these are often associated with changes in soil moisture [60], which can also affect the growth of vegetation [61]. Based on annual temporal Sentinel-2 satellite images, the Normalized Difference Vegetation
Index (NDVI) was computed to eliminate the impact of vegetation on phase decorrelation (coherence loss), as estimated in Section 2.2. Within the Geographic Information System (GIS) environment, an NDVI mask was created, and a threshold of 0.2 was applied to ensure that any areas with an NDVI ≥ 0.2 were excluded from additional investigation. The coherence values, which were determined after the application of this mask, were unaffected by the presence of vegetation.

2.3. Precipitation

Rainfall can alter the moisture content of soil, causing surface deformation such as subsidence or lateral movement of the ground and affecting the soil's ability to swell and shrink. Intense precipitation, which enables the soil to absorb water, resulting in the swelling of expansive soils like clay, may accelerate subsidence by compressing the earth under the pressure of the structures above it. On the other hand, as the soil dries up, it might cause subsidence due to shrinkage. Infrastructure and built-up areas can be seriously endangered by surface deformation in regions with expansive soils and variable moisture levels. Rainfall level datasets were retrieved from 24 weather stations at different elevation levels by the Department of Meteorology, adequately covering our study area (Table 1).

Table 1. Datasets used and their linkage to hazardous deformation/motion zones.

Datasets	Source	Description	Information
Sentinel-1	Copernicus Dataspace Browser	SLC/IW	Time-series of the SAR scenes to determine subsidence/uplift phenomena.
Sentinel-2	Copernicus Dataspace Browser	NDVI	One of the most widely used vegetation indicators that provide information on vegetation condition.
Precipitation	Department of Meteorology	Rainfall datasets	Measurements of precipitation data from meteorological stations.
Soil map	Geological Survey Department	Soil properties	Information about the spatial distribution of different soil types and properties.

Table 1. *Cont.*

Datasets	Source	Description	Information

Geomorphological derivatives	ALOSPalsar DEM (https://search.asf.alaska.edu/#/ (accessed on 4 June 2024))	Topographic Wetness Index	A geomorphometric index that highlights areas that are accumulating moisture.
		Topographic Position Index landform classification	A geomorphometric index that can determine the landform types that could be related to valleys and plains and, by extension, associated with moisture accumulation.
Hydrogeology	Geological Survey Department	Hydrogeological formations	Geological formations were processed to retrieve permeability levels.

2.4. Soil Properties

The phenomena of swelling, shrinking, and surface deformation are significantly influenced by soil properties. The way soil reacts in response to moisture variations is greatly influenced by its mineral composition, texture, and structure. Expansive soils, including clay-rich soils, are more likely to swell and shrink because of their high concentration of clay and small particle size. Due to the high capacity of clay minerals to absorb water, when soil moisture levels increase, soils swell. On the contrary, as water evaporates from the soil substrate during dry periods or when moisture content decreases, clay soils shrink. Significant variations in soil volume due to swelling and/or shrinking may cause lateral displacement, uplift, or subsidence, among other surface deformations. Soil properties were obtained by the Geological Survey Department with a 100 m spatial resolution, including information such as geology and soil texture (Table 1). These soil properties were processed, classifying them based on their swelling or shrinking properties (Appendix A, Table A1).

2.5. Geomorphological Derivatives

Landform derivatives and a variety of geomorphometric analyses were carefully determined using sophisticated methods. The ALOSPalsar DEMs served as the basis of the input data for this analysis. Thus, terrain characteristics may be precisely mapped, leading to better knowledge of how vulnerable the landscape can be to surface deformation phenomena by offering insightful information about the terrain morphology.

The Topographic Wetness Index (TWI) assesses the spatial distribution of soil moisture and surface saturation in relation to topography, utilizing DEMs as described by [62] (Table 1). This index correlates with slope gradients, as water tends to be collected at the base of slopes. Relative soil moisture is influenced by the steepness of the nearby slopes and the drainage patterns. Low TWI values indicate high slope gradients and minimal streamflow accumulation, while high TWI values indicate gentle slope surfaces with significant moisture retention and areas with alluvial depositions [63–65]. Given that topography profoundly influences hydrological processes, TWI serves as a representation of water distribution influenced by terrain [66].

Topographic Position Index (TPI) landform classification consists of 10 landform classes: streams, mid-slope drainage, local ridges, valleys, plains, foot slopes, upper slopes, upland drainage, mid-slope ridges, and high ridges (Table 1). The combination of two distinct neighborhood sizes improves the delineation of complex geomorphological aspects by identifying complicated landscape elements [67]. When one neighborhood size is used, it usually provides only a limited amount of information on the overall structure of the landscape. This comprehensive approach is particularly valuable in understanding surface deformation and swelling phenomena, as it provides detailed information on terrain characteristics, such as slope gradients and drainage patterns, which can influence the susceptibility of landscapes to deformation processes.

2.6. Hydrogeology

The movement and distribution of groundwater within the subsurface can significantly influence soil moisture levels, thereby affecting soil behavior. Expanding soils tend to swell in areas with high groundwater tables or substantial water penetration due to a soil moisture content increase. Swelling occurs because soil particles accumulate water and expand, which may cause the ground to rise. In contrast, soil may shrink as moisture is lost during times of low groundwater

levels or decreased water infiltration, leading to soil consolidation and compaction. As a result, the earth surface may settle or subside.

The hydrogeological map was retrieved by processing the geological maps acquired by the Geological Survey Department with a 100 m spatial resolution containing geological information, which were converted to hydrogeological formations based on their permeability levels (Table 1). Then, these were reclassified based on their swelling effect (Appendix A, Table A2).

2.7. GIS-Based Multi-Criteria Decision Analysis (MCDA)

The integration of GIS-based MCDA provides a robust framework to assess and manage the swelling and shrinking effects that significantly impact ground stability. This comprehensive analysis involved the consideration of multiple factors, including soil properties, precipitation, geomorphological derivatives, hydrogeology, and remote sensing data. The outcomes of the diverse methodological approaches described earlier in conjunction with the auxiliary datasets, presented in Table 1, were implemented within an MCDA procedure.

All factors were considered to be a set of alternatives, which are assessed based on several evaluation criteria that may conflict or have varying importance [68]. The MCDA steps followed were based on previous GIS-based MCDA studies integrating geographical data and assessing their importance to retrieve the overall decision criteria assessment [69,70].

However, there are certain constraints in the use of GIS-based MCDA procedures [71]. AHP is a structured decision-making approach that can effectively address issues associated with conflicting criteria, varying importance, and subjective judgments for diverse decisionmaking problems [72]. The process involves constructing a hierarchy of criteria, assigning weights to these criteria based on pairwise comparisons, and then synthesizing the results to determine the overall rankings of the alternatives [73].

Moreover, a Consistency Ratio (CR) was used to check the results' consistency, with $CR < 0.1$ indicating a reasonable level of consistency in the pairwise comparison, while $CR > 0.1$ requires revision of the judgements for acceptable inconsistency. This hierarchical structure allows for a clear understanding of the influence of each criterion and the relative importance of alternatives. The combination of weighted criteria, derived from the AHP in this study, allowed an analysis of the relationships between the various factors affecting ground stability.

The final step was to synthesize these weighted criteria to produce a composite score for each alternative, providing a clear and justifiable assessment of phenomena related to ground displacement [42,74]. This comprehensive AHP-based MCDA approach resulted in standardized scores that can be used to prioritize and address issues associated with ground stability in relation to swelling and shrinking effects [44,75].

2.8. Accuracy Assessment

To evaluate the performance of the MCDA outcome, an accuracy assessment and validation procedure was conducted. This procedure was based on the acknowledgement of ground-truth observations and the outcomes of Persistent Scatterer Interferometry (PSI) following the recent study of [53]. In the present study, PSI analysis was applied to 139 images of the descending track 167. InSAR time-series analysis on images obtained from 2016 to 2022 was performed to assess Line of Sight ground displacements. Sentinel-1 data, covering Cyprus, were downloaded from the Hellenic Mirror Site and the Sentinel Greek Copernicus Data Hubs (https://sentinels.space.noa.gr (accessed on 20 June 2024)).

The scene of 12 April 2019 was used as the primary image for the PSI analysis, based on the minimum spatial and temporal decorrelation of the interferometric stack of Sentinel1 images. The P-PSI [76,77] processing chain, a fully automated, parallelized version of PSI that is developed and operates at the Operational Unit BEYOND Centre for Earth Observation Research and Satellite Remote Sensing of the Institute for Astronomy and Astrophysics, Space Applications and Remote Sensing of the National Observatory of Athens, was employed for PSI analysis. Line of Sight displacements were estimated using the open-source software ISCE [78] to create an interferometric stack and StaMPS [79] for the PSI analysis. Finally, atmospheric corrections were applied using the open-source Toolbox for Reducing Atmospheric InSAR Noise (TRAIN) [80]. More detailed information on the methodological workflow and stages can be found in [65].

The overall assessment of agreement between the MCDA and PSI (LOS displacements were interpolated using the Inverse Distance Weighting (IDW) algorithm) outcomes involved a total number of 75 random points, consisting of 15 sample points for each class of the MCDA outcome. Then, based on stratified random selection, 40% from the total random points were used for validation and accuracy assessment, allowing us to measure the level of agreement between MCDA and PSI ranking classes using overall accuracy (OA) and Kappa statistics [81]. In addition, ground-truth validation observations took place to detect deformed/affected structures in the broader area of Pyrgos and Parekklisia in Cyprus.

3. Results

The results of the various methodological steps, presented previously in detail, are included in this section.

3.1. Coherent Change Detection (CCD)

The CCD data analysis revealed significant noise in the coherence difference data, rendering them unsuitable for further analysis. However, the normalized coherence difference proved effective in significantly reducing the "noise" in most cases, resulting in a classification based on each image's mean value and standard deviation.

Figure 5 shows the results for the ascending and descending satellite images from Pyrgos–Parekklisia area, whereas Figure 6 shows the results for the ascending and descending satellite images from the Moni–Monagroulli area, indicating a notable difference between the Coherence Difference (Figure 6a,c) and the Normalized Coherence difference (Figure 6b,d) in each case.

The NDVI was computed using the optical Sentinel-2 images to eliminate the impact of vegetation on phase decorrelation (coherence loss). Any areas with an NDVI ≥ 0.2 were excluded from additional investigation, as shown in Figure 7 below. Thus, only coherence values unaffected by the presence of vegetation were used in the following calculations.

The classification utilizing the deviations from the mean values of the coherence data was applied to all the images for the AoI within a GIS environment, creating a single image for the AoI for all the examined years revealing all the changes that occurred in this time period (Figure 8).

Figure 5. Pyrgos–Parekklisia area. (**a**) Coherence difference and (**b**) Normalized Coherence difference from descending Sentinel-1 satellite images during 12 February 2021–8 March 2021. (**c**) Coherence difference and (**d**) Normalized Coherence difference from ascending Sentinel-1 satellite images during 23 February 2021–7 March 2021.

Figure 6. Moni–Monagroulli area. (**a**) Coherence difference and (**b**) Normalized Coherence difference from descending Sentinel-1 satellite images during 12 February 2021–8 March 2021. (**c**) Coherence difference and (**d**) Normalized Coherence difference from ascending Sentinel-1 satellite images during 23 February 2021–7 March 2021.

Figure 7. Annual NDVI variations and corresponding masked areas excluded from further analysis.

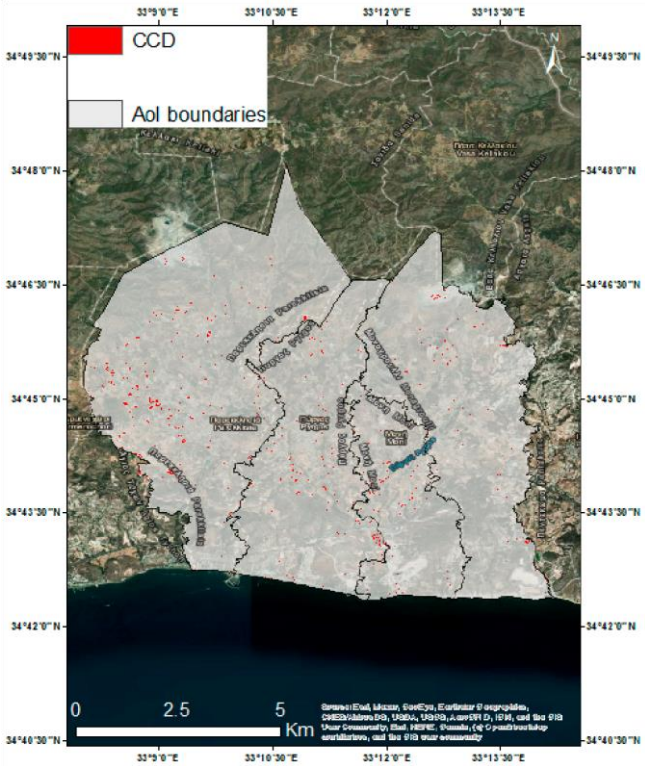

Figure 8. CCD of the Area of Interest showing the changes that occurred between 2016 and 2022.

3.2. Geomorphological Derivatives

The TWI derived from the analysis emphasized the areas of moisture accumulation within the AoI, as depicted in Figure 9. Notably, high levels of moisture accumulation are apparent to the west and southeast of Pyrgos, and to the south of Moni village, coinciding with the presence of Moni formations and olivine-phyric pillow lavas.

Figure 9. The TWI with dark bluish hues highlighting the high moisture accumulation.

Interestingly, these areas exhibit increased levels of moisture accumulation extending beyond the stream network and valleys. These regions, based on derived landform types, are primarily characterized by plains and semi-mountainous areas (Figure 10).

Figure 10. Landform type classification, showing valleys, semi-mountainous, and mountainous zones.

3.3. Precipitation

The precipitation distribution, as derived from 24 weather stations of the Department of Meteorology from different elevations, was determined, as shown in Figure 11 below.

Figure 11. The determined precipitation derived from the weather stations.

3.4. Soil Properties

The soil texture map generated was reclassified to delineate zones based on their swelling potential. Regions exhibiting moderate to high levels of swelling and shrinking effect are observed around Parekklisia, extending westward and southward from Pyrgos, and southward from Moni village. These areas are predominantly characterized by clay and loam texture properties, as presented below in Figure 12. The soil texture map was reclassified to highlight their swelling/shrinking effect (Figure 13).

Figure 12. The soil texture map of the AoI.

Figure 13. The reclassified soil texture map, highlighting the degree of the swelling/shrinking effect.

3.5. Hydrogeology

The hydrogeological map, which was derived from the geological map, was reclassified to emphasize the extent of swelling, as depicted in Figure 14. High levels of swelling are notably observed, in conjunction with areas of high TWI moisture accumulation, to the west and southeast of Pyrgos, as well as in the southern vicinity of Moni village.

Figure 14. The reclassified hydrogeological map highlights the swelling degree.

3.6. GIS-Based MCDA to Assess Swelling and Shrinking Effect

The application of the GIS-based MCDA, using AHP, revealed significant spatial variability in the swelling and shrinking potential across the study area. The weights of the individual factors are presented below in Table 2, while the CR was 0.98, indicating acceptable inconsistency.

Table 2. The individual factors' weights determined within the MCDA procedure, with a CR < 0.1, indicating an acceptable inconsistency level.

Factors	Weights
CCD	0.499
Soil texture	0.177
Hydrogeology	0.137
TWI	0.073
Rainfall	0.073
Landforms	0.041
Consistency ratio (CR)	**0.098**

High-risk zones were identified primarily in regions with clay-rich soils, flat terrain, high TWI values with high moisture accumulation, and significant rainfall variations. These areas correspond to the weathered pillow lavas and bentonitic clays of the Kannaviou and Moni formations, particularly around the Pyrgos and Parekklisia villages.

The spatial distribution of swelling and shrinking risk, as depicted in the resulting maps (Figure 15), underscores the importance of integrating multiple data sources and analytical techniques. The final outcome can serve as a valuable tool for decision-makers, enabling targeted interventions and informed land-use planning. By prioritizing high-risk zones, mitigation measures such as soil stabilization, improved drainage systems, and controlled land-use practices can be effectively implemented to reduce the adverse impacts of ground deformation.

Figure 15. The GIS-based MCDA swelling and shrinking effect outcome based on the acknowledged variables of CCD, soil texture, hydrogeology, TWI, landforms, and rainfall. High-risk zones are presented in orange and very high-risk zones in red.

3.7. Accuracy Assessment

In the accuracy assessment and validation process, the outcomes of the LOS displacements (Figure 16) in Pyrgos and Parekklisia were estimated and acknowledged with the implementation of Persistent Scatterer Interferometry on Sentinel-1 images of a descending satellite pass. A positive displacement trend dominates in the broader area, with a maximum value of 10 mm/y. For a more accurate integration of InSAR and optical data, the LOS displacements were interpolated to have the same pixel size as the CCD results.

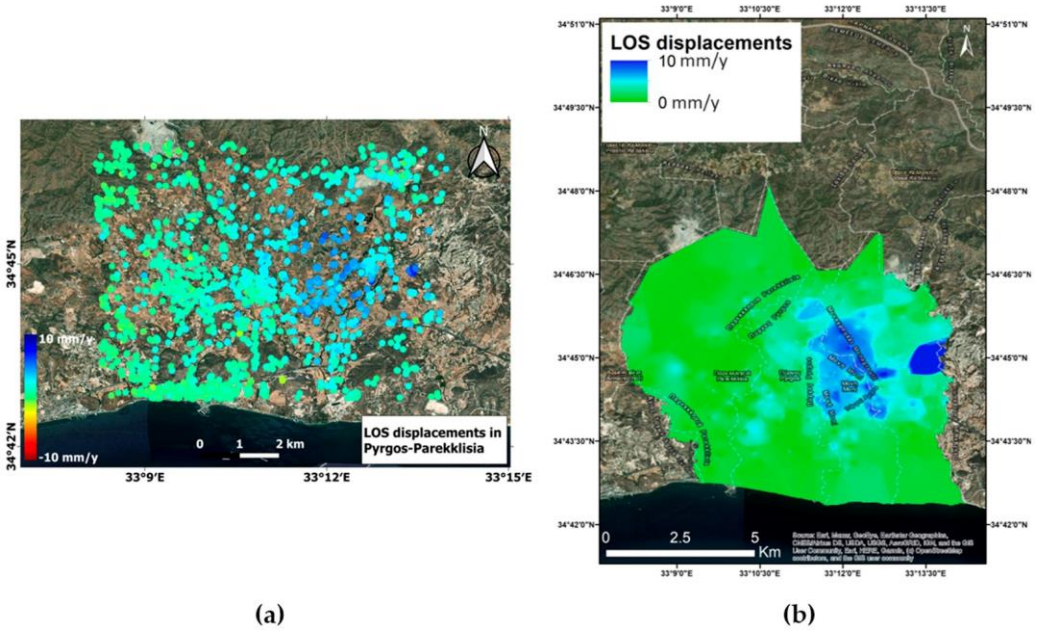

Figure 16. (**a**) Sentinel-1 LoS displacements in Pyrgos–Parekklisia for descending satellite pass and (**b**) interpolated Sentinel-1 LOS displacements in Pyrgos–Parekklisia for descending satellite pass.

The IDW interpolation provided the optimal result, as the deforming areas were preserved without compromising the quality of the final product. Figure 16 presents the interpolated Sentinel-1 LOS displacements as estimated for Pyrgos and Parekklisia. The correlation of the uplift phenomenon identified in the Pyrgos–Parekklisia villages and extreme precipitation events was also studied by using PSI on ascending Sentinel-1 data and ERA-5 precipitation data [53].

In the accuracy assessment procedure, the overall accuracy (OA) reached a percentage of 72.4%, with the Kappa statistic being 0.66, indicating substantial agreement between the MCDA and the PSI products. The individual ranking classes of the 75 random points selected for the accuracy assessment (Appendix A, Figure A1) between the two products (predicted and actual values) are shown on a confusion matrix heatmap highlighting the similar classes among the datasets (Appendix A, Table A3).

The locations of the ten ground-truth observations, where verified deformed structures were observed around the Pyrgos and Parekklisia villages, coincide within the moderateto very high-risk zones of the produced MCDA spatial map. It is noteworthy that the locations, i.e., coordinates, of the ground-truth observations were obtained from a mobile phone at the time of photo acquisition; thus, some minimal errors were introduced in terms of determining the actual position of the deformed structures presented here below.

Of the ten ground-truth locations, two are located within the very high-risk zone, seven are within the high-risk zone, and one is located within the moderate-risk zone. The locations of the ground-truth observations, superimposed on the MCDA swelling/shrinking risk assessment classes, are presented in Figure 17, along with some photographs from the site visit, taken to verify and validate the findings from the MCDA.

Figure 17. The MCDA swelling and shrinking effect outcome with the overlaid ground-truth locations with verified deformed structures, indicated with red arrows, from ground-truth surveys.

4. Discussion

Ground displacement, which includes events like landslides and ground movements (swelling/shrinking) could have an impact on infrastructure, ecosystems, and human populations. Effective hazard reduction and disaster resilience measures need to be implemented to tackle surface deformation processes, especially in the case of Cyprus, a region notable for its geological diversity and susceptibility to geohazards.

Currently, conventional site investigations using boreholes, wells, and inclinometers are used to study such phenomena by the GSD in Cyprus, the national agency and state consultant for geological matters responsible for the investigation and assessment of the geological environment and geohazards, the monitoring and assessment of seismicity, and the assessment of the geological suitability. In fact, some of the data used in the MCDA were kindly provided by the GSD.

The monitoring and evaluation of ground displacement processes is greatly aided by remote sensing techniques, particularly space-based EO technologies. Radar and optical satellite imagery can be used to identify and track ground displacements over large spatial scales and extended times. The freely available Sentinel satellite images, provided by the European Space Agency through the Copernicus program, facilitate the systematic monitoring of large areas irrespective of weather conditions and time during the day, at the same time overcoming inaccessibility limitations that conventional methods encounter. Moreover, remote sensing techniques allow for the study of large areas, reduce processing times and data collection costs, and provide critical information on time to decision and policy makers, as well as other stakeholders and end users.

This study used CCD to evaluate ground displacement in Cyprus. While CCD analysis made it easier to identify sudden land displacement events like earthquakes and landslides, PSI analysis, acknowledged in the validation stage, offered insightful information about long-term ground displacement trends. CCD was used as a single parameter in the MCDA, whereas PSI was used as a means of validation/accuracy assessment of the results, followed by ground-truth observations via site visits carried out in the AoI. Our comprehension of the temporal evolution and spatial distribution of surface deformation features has been improved by the integration of these remote sensing techniques with geomorphological derivatives.

The integration of auxiliary datasets, such as information on soil properties, hydrogeological data, and precipitation, facilitated an in-depth assessment of the factors driving surface deformation processes in Cyprus. Expandable soils with a high percentage of clay are more likely to expand and contract in response to variations in the moisture content of the soil. The correlation between rainfall patterns and soil moisture content emphasizes the role that precipitation plays in triggering surface deformation processes. Strong rainfall events can cause soil swelling in areas with expansive soils, whereas extended dry spells can cause soil shrinkage and sinking. Through the integration of soil characteristics and precipitation information into our research, we were able to clarify the intricate relationship between surface deformation dynamics and hydrological processes in Cyprus.

Additionally, the use of MCDA offered a methodological framework for evaluating the consequences of swelling and shrinking in accordance with different assessment criteria. Decision-makers can reduce the risks associated with surface deformation hazards by prioritizing mitigation actions and land-use planning strategies via the integration of geographical datasets within a GIS-based framework. Because MCDA is spatially explicit, high-risk locations can be identified, and targeted actions can be implemented to improve resilience and lower vulnerability to surface deformation hazards. This is also enhanced by the PSI outcomes in the validation process, which indicate a maximum 10 mm/y displacement rate. These rates are not as high as those observed in the Nicosia (Cyprus) expansive marl formations (seasonal fluctuations around 30–35 mm) [82], but are similar to those of other regions, like in France, with a few tens of millimeters [8,9], all related to swelling effects.

To facilitate the verification of our results, and the complementarity of the CCD and PSI techniques, satellite images acquired during the same period were used in the PSI and CCD analyses carried out in the present study, as well as in a previous study [56] in the same area, as described earlier. Different components of the SAR images were used in the two methodologies, with phase being used in the case of PSI, whereas amplitude/intensity being used in the case of the CCD methodology, enabling us to obtain different attributes and information from these two distinct methodologies. Ground truthing was also carried out through site visits and visual inspections of several locations to verify the obtained results.

An important step forward in geohazard monitoring and risk management has been made with the thorough assessment of the existing space-based EO technologies and their incorporation into a systematic framework for examining surface displacement processes in Cyprus. This study provides improved knowledge of the variables affecting ground displacement, soil moisture dynamics, and swelling/shrinking impacts by utilizing a variety of datasets and approaches.

In Cyprus and other geohazard-prone areas across the world, future research and monitoring activities are essential for creating reliable techniques and mitigation strategies for reducing the effects of surface deformation on ecosystems, infrastructure, and human populations. In the face of changing ground displacement hazards, cooperation between researchers, governmental organizations, and local populations is crucial for hazard reduction and disaster resilience initiatives.

5. Conclusions

To conclude, the present study shows that the determination of swelling/shrinking processes in Cyprus can be effectively assessed by combining remote sensing methods, geospatial data, and GIS-based spatial analysis. This study offers new knowledge of the variables affecting ground motions, soil moisture dynamics, and swelling/shrinking impacts by utilizing a variety of spatial datasets and approaches.

Our results highlight how crucial it is to take geological, hydrological, and environmental elements into account when assessing natural hazards and managing risks. In Cyprus and other geohazard-prone areas across the world, future research and monitoring activities are essential for creating reliable techniques and mitigation plans to lessen the effects of surface deformation on ecosystems, infrastructure, and human populations.

In the near future, there are plans to include additional spatial data in the MCDA methodological framework, and also very high-spatial-resolution remote sensing data, such as those of PlanetScope (Planet Labs, Berlin, Germany) optical satellite images and COSMO-SkyMed SAR (ASI, Rome, Italy) satellite images, to validate the results obtained through the processing of

the free but coarser spatial resolution data provided by the Sentinel satellites. Moreover, decomposition of the PSI results in up–down and east–west components is planned to study the complexity of such phenomena. Last but not least, ways to integrate such results into the MCDA and other machine learning frameworks will be studied further.

Author Contributions: Conceptualization, A.V.A. and M.T.; methodology, A.V.A. and M.T.; software, M.P., C.T., K.F., Z.P.-C., A.V.A. and M.T.; validation, A.V.A., S.A., C.L. and M.T.; formal analysis, A.V.A., M.T., C.L., M.P., C.T. and K.F.; investigation, A.V.A., M.T., S.A. and C.L.; resources, D.G.H., M.T. and C.K.; data curation, M.T. and D.G.H.; writing—original draft preparation, A.V.A., M.P., C.T., K.F. and M.T.; writing—review and editing, A.V.A., S.A. and M.T.; visualization, A.V.A., M.P., C.T., K.F., S.A. and M.T.; supervision, M.T., C.K. and D.G.H.; project administration, M.T.; funding acquisition, D.G.H. All authors have read and agreed to the published version of the manuscript.

Funding: This research was funded by the European Union's Horizon 2020 research and innovation programme under Grant Agreement No. 857510, and by the Government of the Republic of Cyprus through the Directorate General for European Programmes, Coordination and Development The APC was funded by ERATOSTHENES Centre of Excellence.

Data Availability Statement: The original contributions presented in the study are included in the article, further inquiries can be directed to the corresponding author.

Acknowledgments: The authors acknowledge the 'EXCELSIOR': ERATOSTHENES: Excellence Research Centre for Earth Surveillance and Space-Based Monitoring of the Environment H2020 Widespread Teaming project (www.excelsior2020.eu (accessed on 17 July 2024)). The 'EXCELSIOR' project has received funding from the European Union's Horizon 2020 research and innovation programme under Grant Agreement No. 857510, by the Government of the Republic of Cyprus through the Directorate General for European Programmes, Coordination and Development, and by the Cyprus University of Technology. The authors would also like to thank the Geological Survey Department for their collaboration and provision of the data used in this study.

Conflicts of Interest: The authors declare no conflicts of interest. The funders had no role in the design of the study; in the collection, analyses, or interpretation of the data; in the writing of the manuscript; or in the decision to publish the results.

Appendix A

Table A1. The soil texture properties and their ranking with regard to their relevance to the swelling/shrinking effect.

Soil Texture	Water Content Infiltration Rate	Swelling/Shrinking Effect Ranking
Sand	Very high	Low
Loamy sand	High	Low
Sandy loam	Moderate to high	Low
Loam	Low to moderate	Moderate
Clay loam	Moderate	High
Clay	Very low	High
Gravelly sand	Very high	Low
Rock	Low	Very Low

Table A2. The hydrological formations and their ranking with regard to their relevance to the swelling/shrinking effect.

Hydrogeological Formation	Swelling Effect Ranking
Plutonic rocks	Very low
Heavily fractured intrusive rocks	Very low
Unconfined water in marine and terrestrial fanglomerate and terrace formations	Low
Unconfined water generally at shallow depth in connection with riverbeds, deltaic gravel–sand deposits, and estuarine deposits	Low

Unconfined ground water in aquifers of secondary importance of mainly high retentive chalk	Moderate
Ground water in highly retentive rocks, such as chalk interbedded with marls	Moderate
Mamonia complex, including serpentine	High
Volcanics with dominantly submarine pillow lavas, and occasional pockets of highly saline water	High

Table A3. The ranking of classes between the predicted (MCDA) values and the actual observed (PSI) ones (Class 1 is 'Very low', Class 2 is 'Low', Class 3 is 'Moderate', Class 4 is 'High', and Class 5 is 'Very high'. An accompanying confusion matrix heat map highlights the number of similar classes between the two datasets. Darker blue matrix cells indicate a higher number of similar classes, whereas lighter blue matrix cells indicate a lower number of similar classes.

Longitude (WGS 1984)	Latitude (WGS 1984)	MCDA Ranking (Predicted Value)	PSI Ranking (Actual Value)
33.162	34.718	1	1
33.174	34.718	1	1
33.224	34.721	2	2
33.222	34.722	1	1
33.173	34.722	2	2
33.162	34.723	2	2
33.186	34.723	2	2
33.203	34.726	3	3
33.180	34.726	1	1
33.221	34.727	2	2
33.197	34.728	5	1
33.215	34.728	2	2
33.191	34.729	4	4
33.153	34.729	2	2
33.159	34.731	3	1
33.180	34.734	5	2
33.223	34.734	3	3
33.197	34.734	5	5
33.168	34.735	3	1
33.191	34.735	4	1
33.218	34.735	4	4
33.204	34.735	3	3
33.228	34.735	5	1
33.221	34.736	4	4
33.166	34.737	3	3
33.183	34.737	4	4
33.209	34.738	5	5
33.197	34.738	4	4
33.196	34.740	3	3
33.204	34.740	5	5
33.197	34.740	4	4
33.215	34.741	5	5
33.194	34.741	3	3
33.229	34.741	3	3
33.176	34.741	4	2
33.182	34.742	4	1

Table A3. *Cont.*

Longitude (WGS 1984)	Latitude (WGS 1984)	MCDA Ranking (Predicted Value)	PSI Ranking (Actual Value)
33.165	34.742	5	2
33.224	34.742	3	1
33.201	34.742	5	5
33.211	34.743	3	3
33.203	34.743	3	3
33.176	34.744	4	1
33.228	34.744	3	3

33.154	34.744	2	2
33.158	34.745	5	2
33.198	34.745	3	3
33.178	34.746	3	3
33.219	34.746	4	2
33.218	34.748	4	4
33.224	34.748	5	5
33.182	34.748	4	4
33.212	34.749	3	3
33.217	34.750	3	3
33.217	34.752	4	4
33.221	34.757	2	2
33.145	34.759	2	2
33.139	34.760	1	1
33.160	34.762	2	2
33.222	34.763	5	2
33.190	34.764	5	5
33.218	34.765	1	1
33.200	34.767	2	2
33.138	34.767	1	1
33.226	34.768	4	1
33.209	34.770	1	3
33.158	34.772	1	1
33.174	34.773	2	2
33.215	34.774	1	1
33.188	34.775	1	1
33.203	34.775	1	1
33.178	34.776	2	2
33.187	34.778	1	1
33.161	34.779	2	2
33.210	34.779	1	1
33.150	34.781	1	1

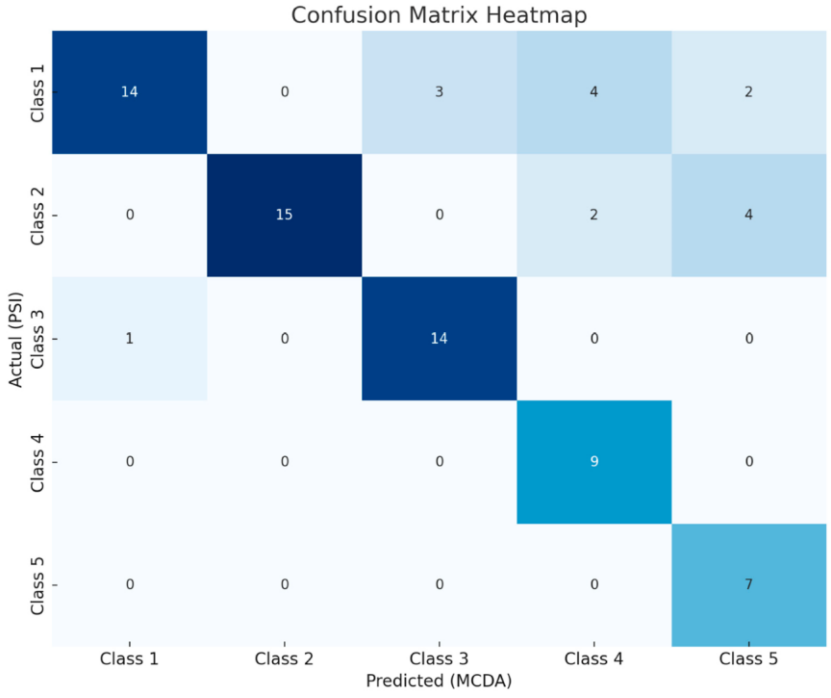

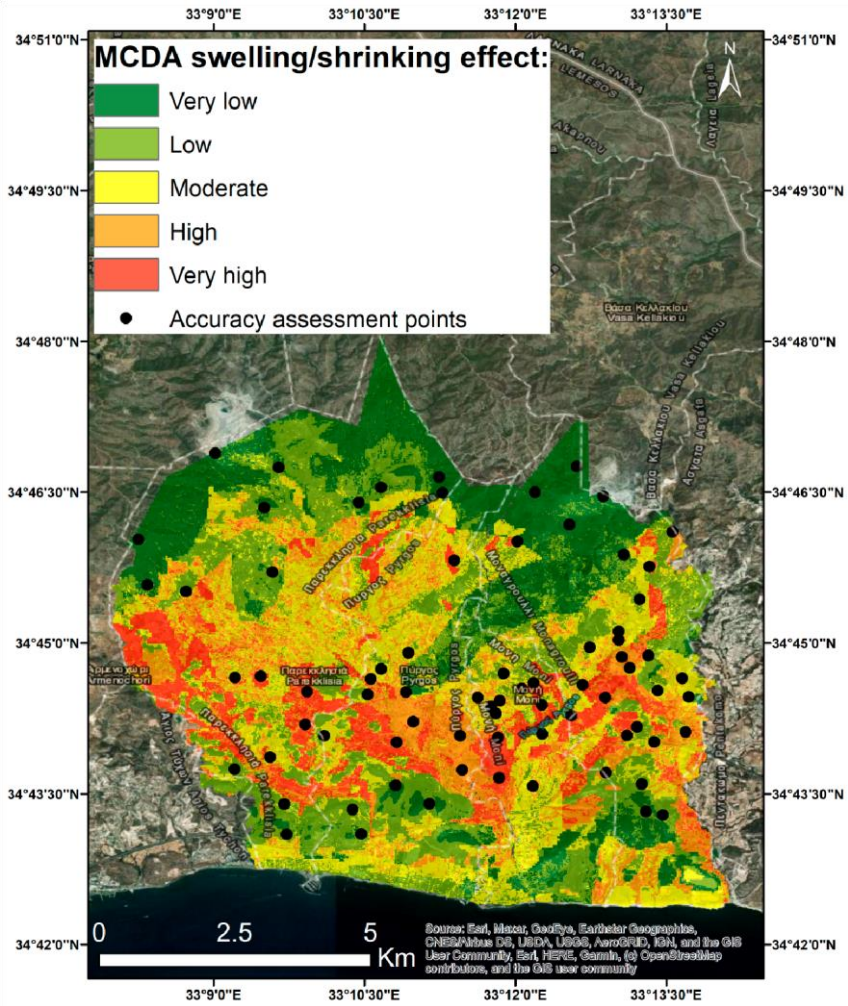

Figure A1. The distribution of the accuracy assessment points across the final MCDA swelling/shrinking effect outcome.

References

1. Messing, I.; Jarvis, N.J. Seasonal Variation in Field-Saturated Hydraulic Conductivity in Two Swelling Clay Soils in Sweden. *J. Soil Sci.* **1990**, *41*, 229–237. [CrossRef]
2. Poulos, H. Parametric Solutions for Strip Footings on Swelling and Shrinking Soils. In Proceedings of the Fifth International Conference on Expansive Soils 1984: Preprints of Papers, Adelaide, Australia, 1 January 1984.
3. Lazarou, G.; Loukidis, D.; Bardanis, M. Moisture Migration Under Mat Foundations in Nicosia Marl. *Geotech. Geol. Eng.* **2019**, *37*, 1585–1608. [CrossRef]
4. Lytton, R. Prediction of Movement in Expansive Clays. In *Vertical and Horizontal Deformations of Foundations and Embankments*; ASCE: Reston, VA, USA, 1994.
5. Chen, Y.; Wei, Y.; Wang, Q.; Chen, F.; Lu, C.; Lei, S. Mapping Post-Earthquake Landslide Susceptibility: A U-Net Like Approach. *Remote Sens.* **2020**, *12*, 2767. [CrossRef]
6. Kaitantzian, A.; Loupasakis, C.; Tzampoglou, P.; Parcharidis, I. Ground Subsidence Triggered by the Overexploitation of Aquifers Affecting Urban Sites: The Case of Athens Coastal Zone along Faliro Bay (Greece). *Geofluids* **2020**, *2020*, e8896907. [CrossRef] 7. Zhao, X.; Chen, W. Optimization of Computational Intelligence Models for Landslide Susceptibility Evaluation. *Remote Sens.* **2020**, *12*, 2180. [CrossRef]
8. Burnol, A.; Foumelis, M.; Gourdier, S.; Deparis, J.; Raucoules, D. Monitoring of Expansive Clays over Drought-Rewetting Cycles Using Satellite Remote Sensing. *Atmosphere* **2021**, *12*, 1262. [CrossRef]
9. Deffontaines, B.; Kaveh, F.; Fruneau, B.; Arnaud, A.; Duro, J. Monitoring Swelling Soils in Eastern Paris (France) Through DinSAR and PSI Interferometry: A Synthesis. In *Engineering Geology for Society and Territory—Volume 5*; Lollino, G., Manconi, A., Guzzetti, F., Culshaw, M., Bobrowsky, P., Luino, F., Eds.; Springer: Cham, Switzerland; Torino, Italy, 15–19 September 2014. [CrossRef]
10. Bai, L.; Jiang, L.; Wang, H.; Sun, Q. Spatiotemporal Characterization of Land Subsidence and Uplift (2009–2010) over Wuhan in Central China Revealed by TerraSAR-X InSAR Analysis. *Remote Sens.* **2016**, *8*, 350. [CrossRef]
11. Khorrami, M.; Abrishami, S.; Maghsoudi, Y.; Alizadeh, B.; Perissin, D. Extreme Subsidence in a Populated City (Mashhad) Detected by PSInSAR Considering Groundwater Withdrawal and Geotechnical Properties. *Sci. Rep.* **2020**, *10*, 11357. [CrossRef] 12. Han, Y.; Zou, J.; Lu, Z.; Qu, F.; Kang, Y.; Li, J. Ground Deformation of Wuhan, China, Revealed by Multi-Temporal InSAR Analysis. *Remote Sens.* **2020**, *12*, 3788. [CrossRef]

13. Preiss, M.; Stacy, N.J.S. *Coherent Change Detection: Theoretical Description and Experimental Results*; Defence Science and Technology Organisation Edinburgh (Australia) Intelligence Surveillance and Reconnaissance Div: Edinburgh, Australia, 2006.
14. Washaya, P.; Balz, T.; Mohamadi, B. Coherence Change-Detection with Sentinel-1 for Natural and Anthropogenic Disaster Monitoring in Urban Areas. *Remote Sens.* **2018**, *10*, 1026. [CrossRef]
15. Oxoli, D.; Boccardo, P.; Brovelli, M.A.; Molinari, M.E.; Monti Guarnieri, A. Coherent Change Detection for repeated-Pass Interferometric Sar Images: An Application to Earthquake Damage Assessment on Buildings. *Int. Arch. Photogramm. Remote Sens. Spat. Inf. Sci.* **2018**, *XLII-3-W4*, 383–388. [CrossRef]
16. Guida, L.; Boccardo, P.; Donevski, I.; Lo Schiavo, L.; Molinari, M.E.; Monti-Guarnieri, A.; Oxoli, D.; Brovelli, M.A. Post-Disaster Damage Assessment through Coherent Change Detection on Sar Imagery. *Int. Arch. Photogramm. Remote Sens. Spat. Inf. Sci.* **2018**, *XLII–3*, 431–436. [CrossRef]
17. Jung, J.; Yun, S.-H. Evaluation of Coherent and Incoherent Landslide Detection Methods Based on Synthetic Aperture Radar for Rapid Response: A Case Study for the 2018 Hokkaido Landslides. *Remote Sens.* **2020**, *12*, 265. [CrossRef]
18. Kontoes, C.H.; Alatza, S.; Chousianitis, K.; Svigkas, N.; Loupasakis, C.; Atzori, S.; Apostolakis, A. Coseismic Surface Deformation, Fault Modeling, and Coulomb Stress Changes of the March 2021 Thessaly, Greece, Earthquake Sequence Based on InSAR and GPS Data. *Seismol. Res. Lett.* **2022**, *93*, 2584–2598. [CrossRef]
19. Papadopoulos, G.A.; Karastathis, V.; Kontoes, C.; Charalampakis, M.; Fokaefs, A.; Papoutsis, I. Crustal Deformation Associated with East Mediterranean Strike–Slip Earthquakes: The 8 June 2008 Movri (NW Peloponnese), Greece, Earthquake (Mw6.4). *Tectonophysics* **2010**, *492*, 201–212. [CrossRef]
20. Bignami, C.; Antonioli, A.; Atzori, S.; Kiratzi, A.; Polcari, M.; Svigkas, N.; Tolomei, C.; Laboratory, G. Mapping InSAR Deformation of Low and Moderate Earthquakes. *Procedia Comput. Sci.* **2021**, *181*, 214–219. [CrossRef]
21. Yi, Y.; Xu, X.; Xu, G.; Gao, H. Landslide Detection Using Time-Series InSAR Method along the Kangding-Batang Section of Shanghai-Nyalam Road. *Remote Sens.* **2023**, *15*, 1452. [CrossRef]
22. Sykioti, O.; Kontoes, C.C.; Elias, P.; Briole, P.; Sachpazi, M.; Paradissis, D.; Kotsis, I. Ground Deformation at Nisyros Volcano (Greece) Detected by ERS-2 SAR Differential Interferometry. *Int. J. Remote Sens.* **2003**, *24*, 183–188. [CrossRef]
23. Hooper, A.; Wright, T.J.; Weiss, J.R.; Rollins, C.; Gaddes, M.; Lazecky, M.; Morishita, Y.; Walters, R.J.; Wang, H.; Hussain, E. Exploiting InSAR on a Large Scale for Tectonics and Volcano Monitoring. In Proceedings of the IGARSS 2020–2020 IEEE International Geoscience and Remote Sensing Symposium, Waikoloa, HI, USA, 26 September–2 October 2020; pp. 6857–6858.
24. Alatza, S.; Papoutsis, I.; Paradissis, D.; Kontoes, C.; Papadopoulos, G.A. Multi-Temporal InSAR Analysis for Monitoring Ground Deformation in Amorgos Island, Greece. *Sensors* **2020**, *20*, 338. [CrossRef]
25. Bekaert, D.P.S.; Handwerger, A.L.; Agram, P.; Kirschbaum, D.B. InSAR-Based Detection Method for Mapping and Monitoring Slow-Moving Landslides in Remote Regions with Steep and Mountainous Terrain: An Application to Nepal. *Remote Sens. Environ.* **2020**, *249*, 111983. [CrossRef]
26. Alatza, S.; Papoutsis, I.; Paradissis, D.; Kontoes, C.; Papadopoulos, G.A.; Raptakis, C. InSAR Time-Series Analysis for Monitoring Ground Displacement Trends in the Western Hellenic Arc: The Kythira Island, Greece. *Geosciences* **2020**, *10*, 293. [CrossRef]
27. Nefros, C.; Alatza, S.; Loupasakis, C.; Kontoes, C. Persistent Scatterer Interferometry (PSI) Technique for the Identification and Monitoring of Critical Landslide Areas in a Regional and Mountainous Road Network. *Remote Sens.* **2023**, *15*, 1550. [CrossRef]
28. Kontoes, C.; Loupasakis, C.; Papoutsis, I.; Alatza, S.; Poyiadji, E.; Ganas, A.; Psychogyiou, C.; Kaskara, M.; Antoniadi, S.; Spanou, N. Landslide Susceptibility Mapping of Central and Western Greece, Combining NGI and WoE Methods, with Remote Sensing and Ground Truth Data. *Land* **2021**, *10*, 402. [CrossRef]
29. Du, J.; Li, Z.; Song, C.; Zhu, W.; Ji, Y.; Zhang, C.; Chen, B.; Su, S. InSAR-Based Active Landslide Detection and Characterization Along the Upper Reaches of the Yellow River. *IEEE J. Sel. Top. Appl. Earth Obs. Remote Sens.* **2023**, *16*, 3819–3830. [CrossRef]
30. Meldebekova, G.; Yu, C.; Li, Z.; Song, C. Quantifying Ground Subsidence Associated with Aquifer Overexploitation Using Space-Borne Radar Interferometry in Kabul, Afghanistan. *Remote Sens.* **2020**, *12*, 2461. [CrossRef]
31. Bockstiegel, M.; Richard-Cerda, J.C.; Muñoz-Vega, E.; Haghighi, M.H.; Motagh, M.; Lalehzari, R.; Schulz, S. Simulation of Present and Future Land Subsidence in the Rafsanjan Plain, Iran, Due to Groundwater Overexploitation Using Numerical Modeling and InSAR Data Analysis. *Hydrogeol. J.* **2024**, *32*, 289–305. [CrossRef]
32. Castellazzi, P.; Garfias, J.; Martel, R.; Brouard, C.; Rivera, A. InSAR to Support Sustainable Urbanization over Compacting Aquifers: The Case of Toluca Valley, Mexico. *Int. J. Appl. Earth Obs. Geoinf.* **2017**, *63*, 33–44. [CrossRef]
33. Marchamalo-Sacristán, M.; Ruiz-Armenteros, A.M.; Lamas-Fernández, F.; González-Rodrigo, B.; Martínez-Marín, R.; DelgadoBlasco, J.M.; Bakon, M.; Lazecky, M.; Perissin, D.; Papco, J.; et al. MT-InSAR and Dam Modeling for the Comprehensive Monitoring of an Earth-Fill Dam: The Case of the Benínar Dam (Almería, Spain). *Remote Sens.* **2023**, *15*, 2802. [CrossRef]
34. Fotiou, K.; Kakoullis, D.; Pekri, M.; Melillos, G.; Brcic, R.; Eineder, M.; Hadjimitsis, D.G.; Danezis, C. Space-Based Displacement Monitoring of Coastal Urban Areas: The Case of Limassol's Coastal Front. *Remote Sens.* **2022**, *14*, 914. [CrossRef]
35. Hooper, A.; Zebker, H.; Segall, P.; Kampes, B. A New Method for Measuring Deformation on Volcanoes and Other Natural Terrains Using InSAR Persistent Scatterers. *Geophys. Res. Lett.* **2004**, *31*. [CrossRef]
36. Kulsoom, I.; Hua, W.; Hussain, S.; Chen, Q.; Khan, G.; Shihao, D. SBAS-InSAR Based Validated Landslide Susceptibility Mapping along the Karakoram Highway: A Case Study of Gilgit-Baltistan, Pakistan. *Sci. Rep.* **2023**, *13*, 3344. [CrossRef]
37. Hussain, S.; Pan, B.; Afzal, Z.; Ali, M.; Zhang, X.; Shi, X.; Ali, M. Landslide Detection and Inventory Updating Using the Time-Series InSAR Approach along the Karakoram Highway, Northern Pakistan. *Sci. Rep.* **2023**, *13*, 7485. [CrossRef]

38. Spaans, K.; Hooper, A. InSAR Processing for Volcano Monitoring and Other Near-Real Time Applications. *J. Geophys. Res. Solid. Earth* **2016**, *121*, 2947–2960. [CrossRef]
39. Alipour, S.; Motgah, M.; Sharifi, M.A.; Walter, T.R. InSAR Time Series Investigation of Land Subsidence Due to Groundwater Overexploitation in Tehran, Iran. In Proceedings of the 2008 Second Workshop on Use of Remote Sensing Techniques for Monitoring Volcanoes and Seismogenic Areas, Napoli, Italy, 11–14 November 2008; pp. 1–5.
40. Chopra, R.; Dhiman, R.D.; Sharma, P.K. Morphometric Analysis of Sub-Watersheds in Gurdaspur District, Punjab Using Remote Sensing and GIS Techniques. *J. Indian Soc. Remote Sens.* **2005**, *33*, 531–539. [CrossRef]
41. Argyriou, A.V.; Teeuw, R.M.; Rust, D.; Sarris, A. GIS Multi-Criteria Decision Analysis for Assessment and Mapping of Neotectonic Landscape Deformation: A Case Study from Crete. *Geomorphology* **2016**, *253*, 262–274. [CrossRef]
42. Segura, F.S.; Pardo-Pascual, J.E.; Rosselló, V.M.; Fornós, J.J.; Gelabert, B. Morphometric indices as indicators of tectonic, fluvial and karst processes in calcareous drainage basins, South Menorca Island, Spain. *Earth Surf. Process. Landf.* **2007**, *32*, 1928–1946. [CrossRef]
43. Chakhar, S.; Martel, J.-M. Enhancing Geographical Information Systems Capabilities with Multi-Criteria Evaluation Functions. *J. Geogr. Inf. Decis. Anal.* **2003**, *7*, 47–71.
44. Drobne, S.; Lisec, A. Multi-Attribute Decision Analysis in GIS: Weighted Linear Combination and Ordered Weighted Averaging. *Information* **2009**, *33*, 459–474.
45. Malczewski, J. GIS-based Multicriteria Decision Analysis: A Survey of the Literature. *Int. J. Geogr. Inf. Sci.* **2006**, *20*, 703–726. [CrossRef]
46. Karnatak, H.C.; Saran, S.; Bhatia, K.; Roy, P.S. Multicriteria Spatial Decision Analysis in Web GIS Environment. *Geoinformatica* **2007**, *11*, 407–429. [CrossRef]
47. Chen, Y.; Khan, S.; Paydar, Z. To Retire or Expand? A Fuzzy GIS-Based Spatial Multi-Criteria Evaluation Framework for Irrigated Agriculture. *Irrig. Drain.* **2010**, *59*, 174–188. [CrossRef]
48. Stow, D.A.V.; Braakenburg, N.E.; Xenophontos, C. The Pissouri Basin Fan-Delta Complex, Southwestern Cyprus. *Sediment. Geol.* **1995**, *98*, 245–262. [CrossRef]
49. Alexandris, A.; Griva, I.; Abarioti, M. Remediation of the Pissouri Landslide in Cyprus. *ISSMGE Int. J. Geoeng. Case Hist.* **2017**, *4*, 14–28. [CrossRef]
50. Danezis, C.; Kakoullis, D.; Fotiou, K.; Pekri, M.; Chatzinikos, M.; Kotsakis, C.; Brcic, R.; Eineder, M.; Nikolaidis, M.; Ioannou, G.; et al. CyCLOPS: A National Integrated GNSS/InSAR Strategic Research Infrastructure for Monitoring Geohazards and Forming the Next Generation Datum of the Republic of Cyprus. In Proceedings of the Geodesy for a Sustainable Earth: Proceedings of the 2021 Scientific Assembly of the International Association of Geodesy, Beijing, China, 28 June–2 July 2021; Springer International Publishing: Cham, Switzerland, 2022; pp. 289–302, ISBN 978-3-031-29506-5.
51. Tzouvaras, M.; Danezis, C.; Hadjimitsis, D.G. Differential SAR Interferometry Using Sentinel-1 Imagery-Limitations in Monitoring Fast Moving Landslides: The Case Study of Cyprus. *Geosciences* **2020**, *10*, 236. [CrossRef]
52. Tzouvaras, M.; Danezis, C.; Hadjimitsis, D.G. Small Scale Landslide Detection Using Sentinel-1 Interferometric SAR Coherence. *Remote Sens.* **2020**, *12*, 1560. [CrossRef]
53. Tzouvaras, M. Statistical Time-Series Analysis of Interferometric Coherence from Sentinel-1 Sensors for Landslide Detection and Early Warning. *Sensors* **2021**, *21*, 6799. [CrossRef]
54. Tzouvaras, M.; Alatza, S.; Prodromou, M.; Theocharidis, C.; Fotiou, K.; Argyriou, A.; Loupasakis, C.; Apostolakis, A.; Pittaki, Z.; Kaskara, M.; et al. Synergy of Advanced Processing Techniques Using Copernicus SAR and Optical Satellite Imagery to Detect Ground Displacements: The Case Studies of Pyrgos and Parekklisia Villages in Cyprus. *Int. Arch. Photogramm. Remote Sens. Spat. Inf. Sci.* **2023**, *XLVIII-1-W2-2023*, 1581–1587. [CrossRef]
55. Alatza, S.; Loupasakis, C.; Apostolakis, A.; Tzouvaras, M.; Themistocleous, K.; Kontoes, C.; Danezis, C.; Hadjimitsis, D.G. Surface Displacements Monitoring in Cyprus via InSAR and Field Investigation: The Case Studies of Pyrgos-Parekklisia and Pedoulas Villages. *Remote Sens.* **2024**, *16*, 960. [CrossRef]
56. Tschernich, R.W. *Zeolites of the World*; Geoscience Press: Totnes, UK, 1992; ISBN 978-0-945005-07-0.
57. Geological Survey Department. Available online: http://www.moa.gov.cy/moa/gsd/gsd.nsf/dmlindex_en/dmlindex_en? opendocument (accessed on 15 April 2024).
58. Bathrellos, G.D.; Koukouvelas, I.K.; Skilodimou, H.D.; Nikolakopoulos, K.G.; Vgenopoulos, A.-L. Landslide Causative Factors Evaluation Using GIS in the Tectonically Active Glafkos River Area, Northwestern Peloponnese, Greece. *Geomorphology* **2024**, *461*, 109285. [CrossRef]
59. Papoutsis, I.; Kontoes, C.; Alatza, S.; Apostolakis, A.; Loupasakis, C. InSAR Greece with Parallelized Persistent Scatterer Interferometry: A National Ground Motion Service for Big Copernicus Sentinel-1 Data. *Remote Sens.* **2020**, *12*, 3207. [CrossRef] 60. Rosen, P.A.; Gurrola, E.; Sacco, G.F.; Zebker, H. The InSAR Scientific Computing Environment. In Proceedings of the EUSAR 2012 9th European Conference on Synthetic Aperture Radar, Nuremberg, Germany, 23–26 April 2012; pp. 730–733.
61. Bekaert, D.; Walters, R.; Wright, T.; Hooper, A.; Parker, D. Statistical Comparison of InSAR Tropospheric Correction Techniques. *Remote Sens. Environ.* **2015**, *170*, 40–47. [CrossRef]
62. Braun, A.; Veci, L. *TOPS Interferometry Tutorial*; ESA: Paris, France, 2021.
63. Bansal, V.; Jagadisan, S.; Sen, J. Chapter 16—Understanding the Urbanization Induced Issues in Mountainous Ecosystems of India: A Comparative Study between Nilgiris (Tamil Nadu), and Lower Himalayas (Uttarakhand), India. In *Understanding Soils of Mountainous Landscapes*; Bhadouria, R., Singh, S., Tripathi, S., Singh, P., Eds.; Elsevier: Amsterdam, The Netherlands, 2023; pp. 303–323, ISBN 978-0-323-95925-4.

64. Mullapudi, A.; Vibhute, A.; Mali, S.; Patil, C. A Review of Agricultural Drought Assessment with Remote Sensing Data: Methods, Issues, Challenges and Opportunities. *Appl. Geomat.* **2022**, *15*, 3. [CrossRef]
65. Tucker, C.J. Red and Photographic Infrared Linear Combinations for Monitoring Vegetation. *Remote Sens. Environ.* **1979**, *8*, 127–150. [CrossRef]
66. Issa, K. Influence of Moisture on Soil Swelling. *Soil. Mech. Found. Eng.* **1997**, *34*, 139–143. [CrossRef]
67. Sharma, S.B.; Kumar, S.; Ovung, E.Y.; Konsam, B. Vegetation Dynamics and Soil Nutrients across Different Shifting Cultivation Fallows in Montane Subtropical Forest of Mizoram, NE India. *Acta Oecologica* **2022**, *115*, 103833. [CrossRef]
68. Beven, K.J.; Kirkby, M.J. A Physically Based, Variable Contributing Area Model of Basin Hydrology/Un Modèle à Base Physique de Zone d'appel Variable de l'hydrologie Du Bassin Versant. *Hydrol. Sci. Bull.* **1979**, *24*, 43–69. [CrossRef]
69. Schmidt, F.; Persson, A. Comparison of DEM Data Capture and Topographic Wetness Indices. *Precis. Agric.* **2003**, *4*, 179–192. [CrossRef]
70. Conoscenti, C.; Di Maggio, C.; Rotigliano, E. Soil Erosion Susceptibility Assessment and Validation Using a Geostatistical Multivariate Approach: A Test in Southern Sicily. *Nat. Hazards* **2008**, *46*, 287–305. [CrossRef]
71. Migon´, P. Weathering and Hillslope Development. *Treatise Geomorphol.* **2013**, *4*, 159–178. [CrossRef]
72. Hjerdt, K.N.; McDonnell, J.J.; Seibert, J.; Rodhe, A. A New Topographic Index to Quantify Downslope Controls on Local Drainage. *Water Resour. Res.* **2004**, *40*. [CrossRef]
73. Tagil, S.; Jenness, J. GIS-Based Automated Landform Classification and Topographic, Landcover and Geologic Attributes of Landforms Around the Yazoren Polje, Turkey. *J. Appl. Sci.* **2008**, *8*. [CrossRef]
74. Boroushaki, S.; Malczewski, J. Implementing an Extension of the Analytical Hierarchy Process Using Ordered Weighted Averaging Operators with Fuzzy Quantifiers in ArcGIS. *Comput. Geosci.* **2008**, *34*, 399–410. [CrossRef]
75. Nyimbili, P.H.; Erden, T. GIS-Based Fuzzy Multi-Criteria Approach for Optimal Site Selection of Fire Stations in Istanbul, Turkey. *Socio-Econ. Plan. Sci.* **2020**, *71*, 100860. [CrossRef]
76. Saaty, T.L. A Scaling Method for Priorities in Hierarchical Structures. *J. Math. Psychol.* **1977**, *15*, 234–281. [CrossRef] 77. Saaty, T.L.; Vargas, L. *Prediction, Projection and Forecasting*; Kluwer Academic: Dordrecht, The Netherlands, 1991.
78. Malczewski, J. GIS-Based Land-Use Suitability Analysis: A Critical Overview. *Prog. Plan.* **2004**, *62*, 3–65. [CrossRef]
79. Kaya, I.; Çolak, M.; Terzi, F. A Comprehensive Review of Fuzzy Multi Criteria Decision Making Methodologies for Energy Policy˙ Making. *Energy Strategy Rev.* **2019**, *24*, 207–228. [CrossRef]
80. Raines, K.S.; Salha, S.; Sandberg, R.L.; Jiang, H.; Rodríguez, J.A.; Fahimian, B.P.; Kapteyn, H.C.; Du, J.; Miao, J. Three-Dimensional Structure Determination from a Single View. *Nature* **2010**, *463*, 214–217. [CrossRef]
81. Feng, Z.; Zhang, H.; Duan, J.; He, L.; Yuan, X.; Gao, Y.; Liu, W.; Li, X.; Feng, W. Improved Spectral Detection of Nitrogen Deficiency and Yellow Mosaic Disease Stresses in Wheat Using a Soil Effect Removal Algorithm and Machine Learning. *Remote Sens.* **2023**, *15*, 2513. [CrossRef]
82. Tzampoglou, P.; Loukidis, D.; Koulermou, N. Seasonal Ground Movement Due to Swelling/Shrinkage of Nicosia Marl. *Remote Sens.* **2022**, *14*, 1440. [CrossRef]